

Abstract

**Measurement of the positive kaon-argon total
hadronic differential cross section in the LArIAT
experiment**

Elena Gramellini

2018

Abstract goes here. Limit 750 words.

Measurement of the positive kaon-argon
total hadronic differential cross section in
the LArIAT experiment

A Dissertation
Presented to the Faculty of the Graduate School
of
Yale University
in Candidacy for the Degree of
Doctor of Philosophy

by
Elena Gramellini

Dissertation Director: Bonnie T. Fleming

Date you'll receive your degree

Copyright © 2017 by Elena Gramellini
All rights reserved.

Contents

Acknowledgements	x
1 Introduction	1
1.1 The Standard Model	1
1.2 Neutrinos: in and beyond the Standard Model	3
1.2.1 Neutrino in the SM	3
1.2.2 Neutrino Oscillations	5
1.3 Beyond the Standard Model	6
2 Liquid Argon Detectors at the Intensity Frontier	8
2.1 The SBN Program	9
2.1.1 SBN Goals	9
2.1.2 Neutrino Interactions and Detection	9
2.2 DUNE	9
2.2.1 DUNE Non-Accelerator Physics Program	9
2.2.2 Rare Decay Searches: Experimental Limit	9
2.2.3 Nucleon Decay Detection in LAr	9
2.3 Liquid Argon Time Projection Chambers at the Intensity Frontier . .	9
2.3.1 Time Projection Chamber	9
2.3.2 Ionization Detectors with Noble Liquids	9
2.3.3 LArTPC: Principles of Operation	9

2.3.4	Liquid Argon Ionization Charge Detection	9
2.3.5	Liquid Argon scintillation Light Detection	9
3	LArIAT: Liquid Argon In A Testbeam	10
3.1	LArIAT & the Intensity Frontier	10
3.2	The Particles Path to LArIAT	10
3.3	LArIAT Tertiary Beam Instrumentation	13
3.3.1	Bending Magnets	13
3.3.2	Multi-Wire Proportional Chambers	15
3.3.3	Time-of-Flight System	16
3.4	In the Cryostat	18
3.4.1	TPC: Charge Collection	18
3.4.2	TPC: Light Collection System	18
3.4.3	Cryogenics and Purity Control	18
3.4.4	TPC: Electric Field Measurement	18
3.5	Trigger and DAQ	18
3.6	Control Systems	18
4	Kaons Interactions in Argon: Cross Section	19
4.1	Literature Review	19
4.2	How to Measure Hadron Cross Section in LArIAT	19
4.2.1	Particle Selection	20
4.2.2	Wire Chamber to TPC Match	20
4.2.3	The Thin Slice Method	20
4.2.4	Procedure testing with truth quantities	23
5	Data Collection	26

6	LArIAT Monte Carlo	27
6.1	Beamline	27
6.1.1	G4Beamline	27
6.1.2	Data Driven MC	27
6.2	TPC MC	27
7	Energy Calibration	28
8	Tracking Optimization	29
8.1	MC sample and WC2TPC match	29
8.2	Wire chamber-to-TPC match	30
8.2.1	Wire chamber-to-TPC match: importance and definition . . .	30
8.2.2	Matching optimization	31
8.2.3	Porting optimization to data	33
9	Kaon Cross Section Measurement	34
A	Measurement of LArIAT Electric Field	35
B	Construction of A Cosmic Ray Tagger for MicroBooNE	43
C	Pion Analysis	44
C.0.1	Data Sample	44
C.0.2	Capture and Decay	44

List of Figures

3.1	Layout of Fermilab Accelerator complex.	12
3.2	Birds eye view of the LArIAT tertiary beamline. In grey: upstream and downstream collimators; in yellow: bending magnets in yellow; in red: wire chambers; in blue: time of flight; in green: liquid argon TPC volume; in maroon: muon range stack.	12
3.3	Magnetic field over current as a function of the current, for one NDB magnet (excitation curve). The data was collected using two Hall probes (blue and green). We fit the readings with a cubic function (black) to average of measurements (red) given in the legend.	14
3.4	One of the four Multi Wire Proportional Chambers (WC) used in the LArIAT tertiary beamline.	15
3.5	Pictures of the TOF system as was deployed during Run-I and Run-II data taking. The left image is of the upstream TOF paddle and the right image is of the downstream TOF paddle	16
4.1	Hadronic cross sections for π^- -Ar (left) and K^+ -Ar (right) implemented in Geant4 10.01.p3 (solid lines) overlaid the true MC cross section as obtained with the sliced TPC method (markers). The total cross section is shown in green, the elastic cross section in blue and the inelastic cross section in red.	25

8.1	Efficiency (left) and purity (right) for wire chamber-to-TPC match as a function of the radius and angle selections.	33
A.1	Drift velocity dependence on electric field for several temperatures. The slope of the line at any one point represents the electron mobility for that given temperature and electric field.	36
A.2	get rid of current line LArIAT HV simple schematics.	37
A.3	the axis is wrong!! Current reading from the Glassman between May 25th and May 30th, 2016 (typical Run-II conditions).	37
A.4	Pictorial representation of the YX view of the TPC. The distance within the anode planes and between the shield plane and the cathode is purposely out of proportion to illustrate the time difference between hits on collection and induction. A ACP track is shown as an example.	41
A.5	Angle definition in the context of LArIAT coordinates system.	41
A.6	Collection plane Δt fit for Run II positive polarity ACP data selected tracks.	42
A.7	Induction plane Δt fit for Run II positive polarity ACP data selected tracks.	42
C.1	True momentum distribution at wire chamber 4 for every simulated pion arriving in the TPC (pink), ending its life in capture (green) or in decay (blue) in the TPC, linear vertical axis on the left, logarithmic on the right.	46
C.2	Survival ratio as a function of selection threshold on true momentum at wire chamber four for every simulated pion arriving in the TPC (pink), capture (green) or in decay (blue).	47

C.3	Ratio between the capture (green) and decay (blue) events over the total number of events as a as a function of the true momentum at wire chamber four.	47
-----	---	----

List of Tables

1.1	SM elementary fermions. The subscripts L and R indicate respectively the negative helicity (left-handed) and the positive helicity (right-handed).	2
A.1	Electric field and drift velocities in LArIAT smaller drift volumes . . .	36
A.2	Δt for the different data samples used for the Anode-Cathode Piercing tracks study.	41
C.1	My caption	45

Acknowledgements

A lot of people are awesome. But not you, who are reading my thesis before it's done.

Chapter 1

Introduction

1.1 The Standard Model

The Standard Model (SM) of particle physics is the most accurate theoretical description of the subatomic world and, more generically, one of the most precisely tested theories in the history of physics. The SM describes the strong, electromagnetic and weak interactions among elementary particles in the framework of quantum field theory, accounting for the unification of electromagnetic and weak interactions for energies above the vacuum expectation value of the Higgs field. The SM does not describe gravity or general relativity.

The Standard Model is a gauge theory based on the local group of symmetry

$$G_{SM} = SU(3)_C \otimes SU(2)_T \otimes U(1)_Y \quad (1.1)$$

where the subscripts indicate the conserved charges: the strong charge, or color C, the weak isospin T (or rather its third component T_3) and the hypercharge Y. These quantities can be related to the electric charge Q through the Gell-Mann-Nishijima relation:

$$Q = \frac{Y}{2} + T_3. \quad (1.2)$$

Generation	I	II	III	T	Y	Q
Leptons	$\begin{pmatrix} \nu_e \\ e \end{pmatrix}_L$	$\begin{pmatrix} \nu_\mu \\ \mu \end{pmatrix}_L$	$\begin{pmatrix} \nu_\tau \\ \tau \end{pmatrix}_L$	$\begin{matrix} 1/2 \\ -1/2 \end{matrix}$	$\begin{matrix} -1 \\ -1 \end{matrix}$	$\begin{matrix} 0 \\ -1 \end{matrix}$
	e_R	μ_R	τ_R	0	-2	1
Quarks	$\begin{pmatrix} u \\ d' \end{pmatrix}_L$	$\begin{pmatrix} c \\ s' \end{pmatrix}_L$	$\begin{pmatrix} t \\ b' \end{pmatrix}_L$	$\begin{matrix} 1/2 \\ -1/2 \end{matrix}$	$\begin{matrix} 1/3 \\ 1/3 \end{matrix}$	$\begin{matrix} 2/3 \\ -1/3 \end{matrix}$
	u_R	c_R	t_R	0	$4/3$	$2/3$
	d'_R	s'_R	b'_R	0	$-2/3$	$-1/3$

Table 1.1: SM elementary fermions. The subscripts L and R indicate respectively the negative helicity (left-handed) and the positive helicity (right-handed).

In the quantum field framework, the elementary particles correspond to the irreducible representations of the G_{SM} symmetry group. In particular, the particles are divided in two categories, fermions and bosons, according to their spin-statistics. Described by the Fermi-Dirac statistics, Fermions have half-integer spin and are sometimes called “matter-particles”. Bosons or “force carriers” have integer spin, follow the Bose-Einstein statistics and mediate the interaction between fermions. The fundamental fermions and their quantum numbers are listed in Tab 1.1.

Quarks can interact via all three the fundamental forces; they are triplets of $SU(3)_C$, that is they can exist in three different colors: $C = R, G, B$. If one chooses a base where u, c and t quarks are simultaneously eigenstates of both the strong and the weak interactions, the remaining eigenstates are usually written as d, s and b for the strong interaction and d', s' and b' for the weak interaction, because the latter ones are the result of a Cabibbo rotation on the first ones. Charged leptons interact via the weak and the electromagnetic forces, while neutrinos only interact via the weak force. The gauge group univocally determines the number of gauge bosons that carry the interaction; the gauge bosons correspond to the generators of

the group: eight gluons (g) for the strong interaction, one photon (γ) and three bosons (W^\pm, Z^0) for the electroweak interaction. A gauge theory by itself can not provide a description of massive particles, but it is experimentally well known that most of the elementary particles have non-zero masses. The introduction of massive fields in the Standard Model lagrangian would make the theory non-renormalizable, and - so far - mathematically impossible to handle. This problem is solved in the Standard Model by the introduction of a scalar iso-doublet $\Phi(x)$, the Higgs field, which gives mass to W^\pm and Z^0 gauge bosons through the electroweak symmetry breaking and to the fermions through Yukawa coupling [1,2].

1.2 Neutrinos: in and beyond the Standard Model

1.2.1 Neutrino in the SM

Neutrino were introduced in the SM as left-handed massless Weyl spinors. The Dirac equation of motion

$$(i\gamma^\mu\partial_\mu - m)\psi = 0 \quad (1.3)$$

for a fermionic field

$$\psi = \psi_L + \psi_R \quad (1.4)$$

is equivalent to the equations

$$i\gamma^\mu\partial_\mu\psi_L = m\psi_R \quad (1.5)$$

$$i\gamma^\mu\partial_\mu\psi_R = m\psi_L \quad (1.6)$$

for the chiral fields ψ_R and ψ_L , whose evolution in space and time is coupled through the mass m . If the fermion is massless, the chiral fields decouple and the fermion can be described by a single Weyl spinor with two independent components. Pauli initially rejected the description of a physical particle through a single Weyl

spinor because of its implication of parity violation. In fact, since the spatial inversion operator throws $\psi_R \leftrightarrow \psi_L$, parity is conserved only if the both the chiral components exist at the same time. **ADD CITATIONS**. For the neutrino introduction in the SM, experiments came in help of the theoretical description: the constraint of parity conservation weakened after Wu's experiment **ADD CITATIONS AND DATES**, there was no experimental indication for massive neutrinos and neutrinos likely interacted only via the left-handed component.

The symmetry group $SU(2)_T \otimes U(1)_Y$ is the only group relevant for neutrino interactions. The SM electroweak lagrangian is the most general renormalizable lagrangian invariant under the local symmetry group $SU(2)_T \otimes U(1)_Y$. The lagrangian couples the weak isotopic spin doublets and singlets described in 1.1 with the gauge bosons A_a^μ ($a = 1, 2, 3$) and B^μ , and Higgs doublet $\Phi(x)$:

$$\begin{aligned}
\mathcal{L} = & i \sum_{\alpha=e,\mu,\tau} \bar{L}'_{\alpha L} \not{D} L'_{\alpha L} + i \sum_{\alpha=1,2,3} \bar{Q}'_{\alpha L} \not{D} Q'_{\alpha L} \\
& + i \sum_{\alpha=e,\mu,\tau} \bar{l}'_{\alpha R} \not{D} l'_{\alpha R} + i \sum_{\alpha=d,s,b} \bar{q}'^D_{\alpha R} \not{D} q'^D_{\alpha R} + i \sum_{\alpha=u,c,t} \bar{q}'^U_{\alpha R} \not{D} q'^U_{\alpha R} \\
& - \frac{1}{4} A_{\mu\nu} A^{\mu\nu} - \frac{1}{4} B_{\mu\nu} B^{\mu\nu} \\
& + (D_\rho \Phi)^\dagger (D^\rho \Phi) - \mu^2 \Phi^\dagger \Phi - \lambda (\Phi^\dagger \Phi)^2 \\
& - \sum_{\alpha,\beta=e,\mu,\tau} \left(Y_{\alpha\beta}^n \bar{L}'_{\alpha L} \Phi l'_{\beta R} + Y_{\alpha\beta}^{n*} \bar{l}'_{\beta R} \Phi^\dagger L'_{\alpha L} \right) \\
& - \sum_{\alpha=1,2,3} \sum_{\beta=d,s,b} \left(Y_{\alpha\beta}^D \bar{Q}'_{\alpha L} \Phi q'^D_{\beta R} + Y_{\alpha\beta}^{D*} \bar{q}'^D_{\beta R} \Phi^\dagger Q'_{\alpha L} \right) \\
& - \sum_{\alpha=1,2,3} \sum_{\beta=u,c,t} \left(Y_{\alpha\beta}^U \bar{Q}'_{\alpha L} \tilde{\Phi} q'^U_{\beta R} + Y_{\alpha\beta}^{U*} \bar{q}'^U_{\beta R} \tilde{\Phi}^\dagger Q'_{\alpha L} \right). \tag{1.7}
\end{aligned}$$

The first two lines of the lagrangian summarize the kinetic terms for the fermionic fields and their coupling to the gauge bosons $A_a^{\mu\nu}$, $B^{\mu\nu}$ ¹. The third line describes

1. In gauge theories the ordinary derivative ∂_μ is substituted with the covariant derivative D_μ . Here $D_\mu = \partial_\mu + ig A_\mu \cdot I + ig' B_\mu \frac{Y}{2}$, where I and Y are the $SU(2)_L$ and $U(1)_Y$ generators, respectively.

the kinetic terms and the self-coupling terms of the gauge bosons. The forth line is the Higgs lagrangian, which results in the spontaneous symmetry breaking. The last three lines describe the Yukawa coupling between fermions and the Higgs field, origin of the fermion's mass.

The coupling between left-handed and right-handed field generates the mass term for fermions. The SM assumes only left-handed components for neutrinos, thus implying zero neutrino mass. Since any linear combination of massless fields results in a massless field, the flavor eigenstates are identical to the mass eigenstates in the SM.

1.2.2 Neutrino Oscillations

The determination of the flavor of a neutrino dynamically arises from the corresponding charged lepton associated in a CC interaction; for example, a ν_e is a neutrino which produces an e^- , a $\bar{\nu}_\mu$ is a neutrino which produces a μ^+ , *etc.* The neutrino flavor eigenstates $|\nu_\alpha\rangle$, with $\alpha = e, \mu, \tau$, are orthogonal to each other and form a base for the the weak interaction matrix.

Overwhelming experimental data show neutrinos change flavor during their propagation. This phenomenon, predicted by Bruno Pontecorvo in 1957, is called “neutrino oscillations” and it is possible only if the flavor eigenstate are not identical to the mass eigenstates. A minimal extension of the Standard Model introduces three mass eigenstates, $|\nu_i\rangle$ ($i = 1, 2, 3$), whose mass m_i is well defined. The unitary Pontecorvo-Maki-Nakagawa-Sakata matrix transforms the spinor wave functions (ψ) of each component between flavor and mass bases as follows

$$\sum \psi_\alpha |\nu_\alpha\rangle = \sum \psi_i |\nu_i\rangle, \rightarrow \psi_\alpha = U_{PMNS} \psi_i, \quad (1.8)$$

with

$$U_{PMNS} = \begin{bmatrix} c_{12} & s_{12} & 0 \\ -s_{12} & c_{12} & 0 \\ 0 & 0 & 1 \end{bmatrix} \begin{bmatrix} c_{13} & 0 & s_{13}e^{-i\delta} \\ 0 & 1 & 0 \\ -s_{13}e^{-i\delta} & 0 & c_{13} \end{bmatrix} \begin{bmatrix} 1 & 0 & 0 \\ 0 & c_{23} & s_{23} \\ 0 & -s_{23} & c_{23} \end{bmatrix} \begin{bmatrix} e^{i\alpha_1} & 0 & 0 \\ 0 & e^{i\alpha_2} & 0 \\ 0 & 0 & 1 \end{bmatrix} \quad (1.9)$$

where c e s stand respectively for cosine and sine of the corresponding mixing angles (θ_{12} , θ_{23} and θ_{13}), δ is the Dirac CP violation phase, α_1 and α_2 is the eventual Majorana CP violation phases.

Experimental results summary

1.3 Beyond the Standard Model

The discovery of neutrino oscillation and its implication of non-zero neutrino mass mark the beginning of a new, exciting era in neutrino physics: the era of physics Beyond the Standard Model (BSM) in the neutrino sector. We are currently searching for new, deeper theories that can accommodate neutrinos with non-zero mass, while remaining consistent with the rest of the Standard Model.

Open Questions in Neutrino Physics

On one hand, the last X decades of experiments in neutrino oscillations brought spectacular advancements in the understanding of the oscillations pattern, measuring the neutrino mixing angles and mass splitting with a precision of less than 10%. On the other, it opened the field for a series of questions needing experimental answers. Critical challenges in the next decade will entail an even deeper understanding of the neutrino mixing pattern, investigation of the neutrino mass origin, neutrino number and nature, and assessing CP violation in the lepton sector.

Following the recommendation of the latest Particle Physics Project Prioritization

Panel [3], the US is dedicating substantial resources to the development of a short- and long- baseline neutrino program to address many of these fundamental questions. This program pivots on the Liquid Argon Time Projection Chamber (LArTPC) detector technology which will be described in 2.

The main goals of these research programs include:

- Assessment of the existence of right-handed sterile neutrinos.
- Determination of the sign of Δm_{13}^2 (or Δm_{23}^2), i.e., the “neutrino mass ordering”.
- Determination of the octant, i.e. whether θ_{23} is maximal.
- Determination the status of CP symmetry in the lepton sector.

Smallness of neutrino masses, link to GUTs

Towards a more fundamental theory

Despite its highly predictive power, a number of conceptual issues arise in the SM which disfavor it to be a good candidate for a fundamental theory.

The SM rather complex group structure, where a gauge group is formed with the direct product of other three groups as shown in eq. 1.1, is unexplained. Also, the SM fails to include a suitable dark matter candidate and a mechanisms that accounts for the baryon asymmetry of the universe. Within the SM, a total of 25 parameters remain seemingly arbitrary and need to be fitted to data: 3 gauge couplings, 9 charged fermion masses, 3 mixing angles and one CP phase in the CKM matrix, the Higgs mass and quartic coupling, θ_{QCD} , 3 neutrino masses, 3 neutrino mixing angles, 1 Dirac phase and, eventually, 2 Majorana phases.

Chapter 2

Liquid Argon Detectors at the Intensity Frontier

In the next few years, LArTPC experiments – such as the Short-Baseline Neutrino program (SBN) and DUNE – will be major players in the intensity frontier field.

2.1 The SBN Program

2.1.1 SBN Goals

2.1.2 Neutrino Interactions and Detection

2.2 DUNE

2.2.1 DUNE Non-Accelerator Physics Program

2.2.2 Rare Decay Searches: Experimental Limit

2.2.3 Nucleon Decay Detection in LAr

2.3 Liquid Argon Time Projection Chambers at the Intensity Frontier

2.3.1 Time Projection Chamber

2.3.2 Ionization Detectors with Noble Liquids

2.3.3 LArTPC: Principles of Operation

2.3.4 Liquid Argon Ionization Charge Detection

Electron Life Time & purity

Space Charge Effect

Recombination Effect

2.3.5 Liquid Argon scintillation Light Detection

LAr Scintillation Process

Wavelength Shifting of LAr Scintillation Light

Chapter 3

LArIAT: Liquid Argon In A Testbeam

3.1 LArIAT & the Intensity Frontier

3.2 The Particles Path to LArIAT

LArIAT's home at Fermilab is the Fermilab Test Beam Facility (FTBF), where the experiment characterizes a beam of charge particles downstream from the Meson Center beam line.

LArIAT's particles history begins in the Fermilab accelerator complex with a beam of protons. The process of protons acceleration develops in gradual stages, see picture 3.2: gaseous hydrogen is ionized in order to form H^- ions; these ions are boosted to 750 keV by a Cockroft-Walton accelerator and injected to the Linac linear accelerator that increases their energy up to 400 MeV; then, H^- ions pass through a carbon foil and lose the two electrons; the resulting protons are then injected into a rapid cycling synchrotron, called Booster; at this stage protons reach 8 GeV of energy and are compacted into bunches; the next stage of acceleration is the Main Injector,

a synchrotron which accelerates the bunches up to 120 GeV; in the Main Injector, several bunches are merged into one and used for the injection in the last stage.

The Fermilab accelerator complex works in supercycles of roughly 60 seconds in duration. The beam is then split by electrostatic septa and delivered at different experimental halls all over the lab. A 120 GeV/ c primary proton beam with variable intensity is extracted in four-second “spills” and sent to the Meson Center beam line. Here, this primary beam is focused onto a tungsten target to create LArIAT’s secondary beam. The composition of the secondary particle beam is mainly positive pions. For the LArIAT data considered in this work the secondary beam peak momentum was fixed at 64 GeV/ c , although the beam is tunable in momentum between 8-80 GeV/ c ; this was deemed a secondary beamline configuration which allowed a stable beam operation of the FTBF. The beam of pions impinges then on a copper target within a steel collimator inside the LArIAT experimental hall (MC7) to create LArIAT tertiary beam, whose geometry in MC7 has been optimized for LArIAT (shown in Fig. 3.2). The steel collimator selects particles produced with a 13° production angle at the target down the beamline. The particles are then bend by 10° through a pair of dipole magnets. Tuning the magnets field intensity results in a range of particle momenta from 0.2 to 1.4 GeV/ c . The tertiary beam composition counts mostly pions and protons with a small fraction of electrons, muons, and kaons present as well. It is the job of the LArIAT beamline detectors to select the particles polarity, to perform particle identification (beamPID) and to measure the momentum of the tertiary beam particles before they get to the LArTPC. The LArIAT detectors are described in the following paragraphs.

Fermilab Accelerator Complex

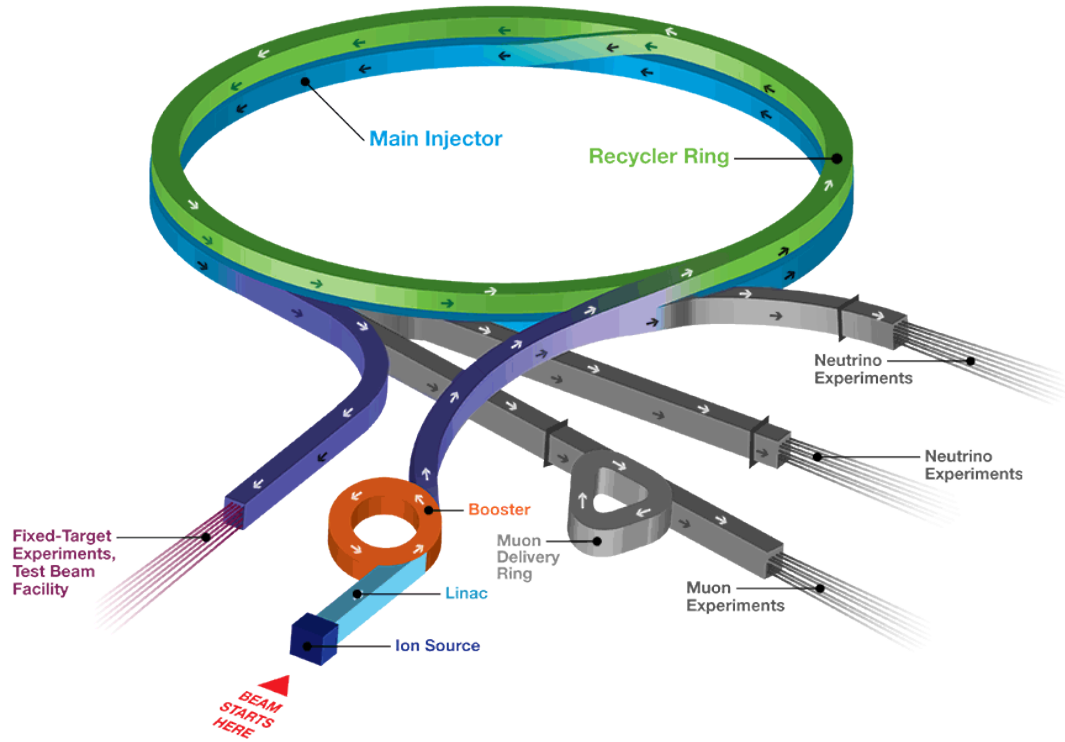


Figure 3.1: Layout of Fermilab Accelerator complex.

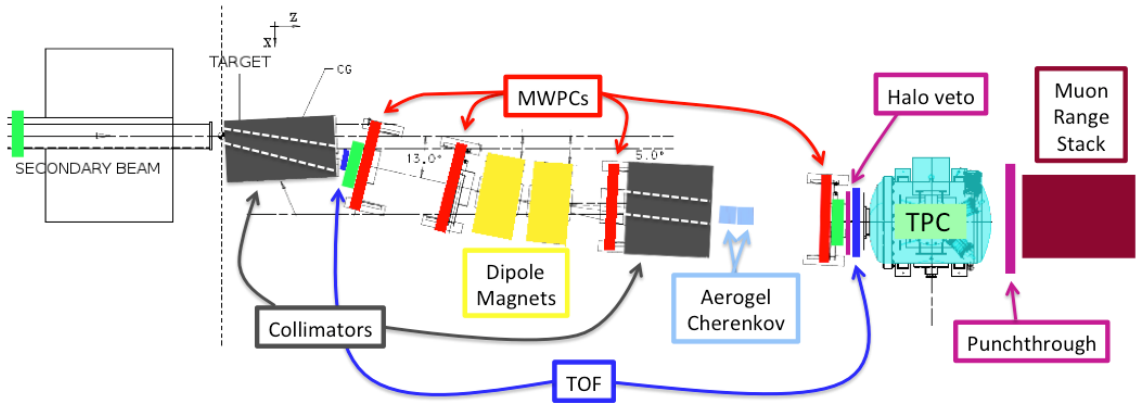


Figure 3.2: Birds eye view of the LArIAT tertiary beamline. In grey: upstream and downstream collimators; in yellow: bending magnets in yellow; in red: wire chambers; in blue: time of flight; in green: liquid argon TPC volume; in maroon: muon range statck.

3.3 LArIAT Tertiary Beam Instrumentation

The instrumentation of LArIAT tertiary beam and the TPC components have changed several times during the three years of LArIAT data taking. The following paragraphs describe the components operational during the data taking period relevant to the hadron cross section measurements (a.k.a. Run II).

The components of the tertiary beamline instrumentation key for the hadron cross section analyses are the target and collimators system, the two bending magnets (in a similar configuration used for the MINERvA T-977 test beam calibration [?]) a set of four wire chambers (WCs) and two time-of-flight scintillating paddles (TOF) and, of course, the LArTPC. The magnets determine the polarity of the particles in the tertiary beam; the combination of magnets and wire chambers determine the particles momentum, which is used to determine the particle species in conjunction with the TOF. A muon range stack downstream from the TPC and two sets of cosmic paddles configured as a telescope surrounding the TPC are also used for calibration purposes.

3.3.1 Bending Magnets

LArIAT uses a pair of identical Fermilab type “NDB” electromagnets, recycled from the Tevatron’s anti-proton ring [CITE CDF?](#). The magnets are a fundamental piece of the LArIAT beamline as they are used in all the three tasks of the LArIAT beamline: the sign of the current in the magnet provide the selection of either positively or negatively charged particles, the value of the magnetic field is used in the momentum determination and the subsequent particle identification.

We describe here the characteristics and response of one magnet. We expect the second one have a similar response, being identical in shape and with a similar history. The magnet aperture measures the gap dimensions to be 14.224 cm of height, 31.75 cm width, and 46.67 cm length. The wire chambers aperture (~ 12.5 cm) is smaller than

the magnet aperture, thus, only the central part of the magnet gap is utilized. The field is extremely uniform over this limited aperture and was measured with two Hall probes, both calibrated with nuclear magnetic resonance probes. The probes measured the excitation curve shown in Figure 3.3.

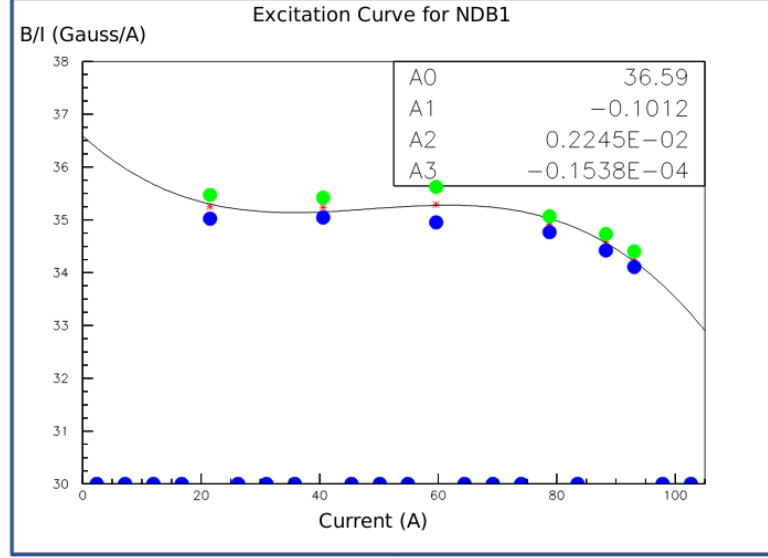


Figure 3.3: Magnetic field over current as a function of the current, for one NDB magnet (excitation curve). The data was collected using two Hall probes (blue and green). We fit the readings with a cubic function (black) to average of measurements (red) given in the legend.

The current being passed through the magnets at a given time is identical in both magnets. For Run II period, the current settings explored were 60A ($B \sim 0.21$ T) and 100A ($B \sim 0.35$ T) in both polarities. Albeit advantageous to enrich the tertiary beam composition with high mass particles such as kaons, we never pushed the magnets current over 100 A, not to incur in overheating. During operation, we operated a air and water cooling system on the magnets and we remotely monitored the magnets temperature.

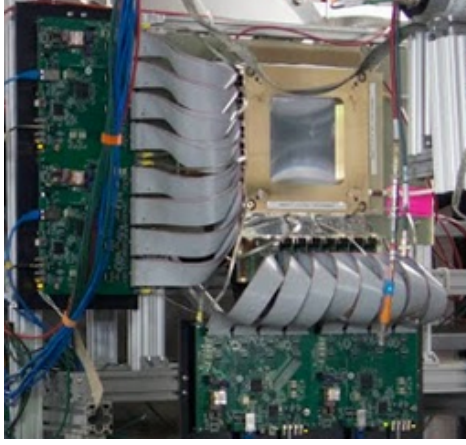


Figure 3.4: One of the four Multi Wire Proportional Chambers (WC) used in the LArIAT tertiary beamline.

3.3.2 Multi-Wire Proportional Chambers

LArIAT uses four Multi-Wire proportional chambers, or wire chambers (WC) for short, two upstream and two downstream from the bending magnets. The geometry of one chamber is shown in Figure 3.4: the WC effective aperture is a square of 12.8 cm perpendicular to the beam direction. Inside the chamber, the 128 horizontal and 128 vertical wires hang at a distance of 1 mm from each other in a mixture of 85% Argon and 15% isobutane gas. The WC operating voltage is between 2400 V and 2500 V. LArIAT wire chambers are an upgraded version of the Fenker Chambers [?], where an extra grounding improves the signal to noise ratio of the electronic readout.

Two ASDQ chips [?] mounted on a mother board plugged into the chamber serve as front end amplifier/discriminator. The chips are connected to a multi-hit TDC [?] which provides a fast OR output used as first level trigger. The TDC time resolution is 1.18 ns/bin and can accept 2 edges per 9 ns. The maximum event rate acceptable by the chamber system is of 1 MHz: this rate is not a limiting factor considering that the rate of the tertiary particle beam at the first wire chamber is estimated to be less than 15 kHz. A full spill of data occurring once per supercycle is stored on the TDC board memory at once and read out by a controller specially designed controller. We use LVDS cables to carry both power and data between the controller and the TDCs

and from the controller to the rest of the DAQ.

Multi-Wire Proportional Chambers functionality

3.3.3 Time-of-Flight System

Two scintillator paddles, one upstream to the first set of WCs and one downstream to the second set of WCs form LArIAT time-of-flight (TOF) detector system.

find exact dimentions The upstream paddle is made of a 10 x 6 x ? cm scintillator piece, read out by two **Hamamatsu 2 inch** PMTs mounted on the beam left side which collect the light from light guides mounted on all four edges of the scintillator. The downstream paddle dimensions are 14 x 14 x ? cm and it is read out by two **Hamamatsu 2 inch** PMTs on the opposite ends of the scintillator. The relatively thin width on the beamline direction minimizes energy loss of the particles coming from the target in the scintillation material.

Figure 3.5: Pictures of the TOF system as was deployed during Run-I and Run-II data taking. The left image is of the upstream TOF paddle and the right image is of the downstream TOF paddle

The CAEN 1751 digitizer is used to digitize the TOF PMTs signals at a sampling rate of 1 GHz. The 12 bit samples are stored in a circular memory buffer. At trigger time, data from the TOF PMTs are recorded to output in a 28.7 μ second windows starting approximately 8.4 μ sec before the trigger time.

TOF functionality

The TOF signals rise time (10-90%) is 4 ns and a full width, half-maximum of 9 ns consistent in time. The signal amplitudes from the upstream TOF and downstream TOF are slightly different: 200 mV for the upstream PMTs but only 50 mV for downstream PMTs.

The time of the pulses was calculated utilizing an oversampled template derived from the data itself. The pulse pedestal was taken from samples far from the pulse

and subtracted to the pulse amplitude. We then stretch vertically a template to match the pedestal-subtracted pulse amplitude and we move it horizontally to find the time. With this technique, we find a pulse time-pickoff resolution better than 100 ps. The pulse pile up is not a significant problem given the TOF timing resolution and the rate of the particle beam. Leveraging on the pulses width uniformity of any given PMT (sigma of 400 ps), we flag events where two pulses overlap as closely in time as 4 ns with an 90% efficiency according to simulation.

We combine the pulses from the two PMTs on each paddle to determine the particles' arrival time by averaging the time measured from the single PMT, so to minimize errors due to optical path differences in the scintillator. However, a time spread of approximately 300 ps is present in both the upstream and downstream detectors, likely due to transit time jitter in the PMTs themselves. There is no evidence of systematic timing drift over long periods such as 3-4 months of a data-taking: the maximum variation of the average time differences between pairs of PMTs reading out the same scintillator is of the order of 150 ps.

3.4 In the Cryostat

3.4.1 TPC: Charge Collection

3.4.2 TPC: Light Collection System

3.4.3 Cryogenics and Purity Control

3.4.4 TPC: Electric Field Measurement

3.5 Trigger and DAQ

3.6 Control Systems

Chapter 4

Kaons Interactions in Argon: Cross Section

4.1 Literature Review

4.2 How to Measure Hadron Cross Section in LAr-IAT

We use both the LArIAT beamline detectors and the LArTPC information in order to measure hadronic cross sections in argon. Albeit with small differences, both the π^- -Ar and K^+ -Ar total hadronic cross section measurements rely on the same procedure described in details in the following paragraphs: we select the particle of interest using a combination of beamline detectors and TPC information (paragraph 4.2.1), we perform a handshake between the beamline information and the TPC tracking to assure we are selecting the right TPC track (paragraph 4.2.2), and we apply the “thin slice” method to get to the final result (paragraph 4.2.3).

4.2.1 Particle Selection

4.2.2 Wire Chamber to TPC Match

After an event passes the selection described in the previous paragraph, we need to identify the track inside the TPC corresponding to the particle which triggered the beamline detectors, a procedure we refer to as “WC to TPC match”. In general, the tracking algorithm will reconstruct more than one track in the event, partially due to the fact that hadrons interact in the chamber, as shown in figure , and partially because of pile up events where the beam of charge particle is too intense compared to the drift time, as shown in figure. **EVENT DISPLAYS**

4.2.3 The Thin Slice Method

Cross Sections on Thin Target

Cross section measurements on a thin target have been the bread and butter of nuclear and particle Iexperimentalists since the Rutherford experiments **NEED CITATION**. At their core, this type of experiments consists in shooting a beam of particles with a known flux on a thin target and recording the outgoing flux.

In general, the target is not a single particle, but rather a slab of material containing many diffusion centers. The so-called “thin target” approximation assumes that the target centers are uniformly distributed in the material and that the target is thin compared to the interaction length so that no center of interaction sits in front of another. In this approximation, the ratio between the number of particles interacting in the target $N_{Interacting}$ and number of incident particles $N_{Incident}$ determines the interaction probability $P_{Interacting}$, which is the complementary to one of the survival probability $P_{Survival}$. Equation 4.1

$$P_{Survival} = 1 - P_{Interacting} = 1 - \frac{N_{Interacting}}{N_{Incident}} = e^{-\sigma_{TOT}n\delta X} \quad (4.1)$$

describes the probability for a particle to survive the thin target. This formula relates the total cross section σ_{TOT} , the density of the target centers n and the thickness of the target along the incident hadron direction δX , to the interaction probability¹. If the target is thin compared to the interaction length of the process considered, we can Taylor expand the exponential function in equation 4.1 and find a simple proportionality relationship between the number of incident and interacting particles, and the cross section, as shown in equation 4.2:

$$1 - \frac{N_{Interacting}}{N_{Incident}} = 1 - \sigma_{TOT} n \delta X + O(\delta X^2). \quad (4.2)$$

Solving for the cross section, we find:

$$\sigma_{TOT} = \frac{1}{n \delta X} \frac{N_{Interacting}}{N_{Incident}}. \quad (4.3)$$

Not-so-Thin Target: Slicing the Argon

The LArIAT TPC, with its 90 cm of length, is not a thin target. **Find expected interaction length for hadrons and kaons.** However, the fine-grained tracking of the LArIAT LArTPC allows us to treat the argon volume as a sequence of many adjacent thin targets.

As described in section 3, LArIAT wire planes count 240 wires each. The wires are oriented at +/- 60° from the vertical direction at 4 mm spacing, while the beam direction is oriented 3 degrees off the z axis in the XZ plane. **review this math** The wires collect signals proportional to the energy loss of the hadron along its path in a $\delta X = 4 \text{ mm} / \sin(60^\circ) \approx 4.7 \text{ mm}$ slab of liquid argon. Thus, one can think to slice the TPC into many thin targets of $\delta X = 4.7 \text{ mm}$ thickness along the direction of the incident particle.

1. The scattering center density in the target, n , relates to the argon density ρ , the Avogadro number N_A and the argon molar mass m_A as $n = \frac{\rho N_A}{m_A}$.

Considering each slice j a “thin target”, we can apply the cross section calculation from Eq. 4.3 iteratively, evaluating the kinetic energy of the hadron as it enters each slice, E_j^{kin} . For each WC-to-TPC matched particle, the energy of the hadron entering the TPC is known thanks to the momentum and mass determination by the tertiary beamline,

$$E_{FrontFace}^{kin} = \sqrt{p_{Beam}^2 - m_{Beam}^2} - E_{loss}, \quad (4.4)$$

where E_{loss} is a correction for the energy loss in the dead material between the beamline and the TPC front face (more on ??). The energy of the hadron at the each slab is determined by subtracting the energy released by the particle in the previous slabs. For example, at the j^{th} point of a track, the kinetic energy will be

$$E_j^{kin} = E_{FrontFace}^{kin} - \sum_{i < j} \Delta E_i, \quad (4.5)$$

where ΔE_i is the energy deposited at each argon slice before the j^{th} point as measured by the calorimetry associated with the tracking.

If the particle enters a slice, it contributes to $N_{Incident}(E^{kin})$ in the energy bin corresponding to its kinetic energy in that slice. If it interacts in the slice, it then also contributes to $N_{Interacting}(E^{kin})$ in the appropriate energy bin. The cross section as a function of kinetic energy, $\sigma_{TOT}(E^{kin})$ will then be proportional to the ratio $\frac{N_{Interacting}(E^{kin})}{N_{Incident}(E^{kin})}$.

The statistical uncertainty for each energy bin is calculated by error propagation from the statistical uncertainty on $N_{Incident}$ and $N_{Interacting}$. Since the number of incident hadrons in each energy bin is given by a simple counting, we assume that $N_{Incident}$ is distributed as a poissonian with mean and σ^2 equal to $N_{Incident}$ in each bin. On the other hand, $N_{Interacting}$ follows a binomial distribution: a particle in a given energy bin might or might not interact. The square of the variance for the

binomial is given by

$$\sigma^2 = \mathcal{N} P_{Interacting} (1 - P_{Interacting}); \quad (4.6)$$

since the interaction probability $P_{Interacting}$ is $\frac{N_{Interacting}}{N_{Incident}}$ and the number of tries \mathcal{N} is $N_{Incident}$, equation 4.6 translates into

$$\sigma^2 = N_{Incident} \frac{N_{Interacting}}{N_{Incident}} \left(1 - \frac{N_{Interacting}}{N_{Incident}}\right) = N_{Interacting} \left(1 - \frac{N_{Interacting}}{N_{Incident}}\right). \quad (4.7)$$

$N_{Incident}$ and $N_{Interacting}$ are not independent. The uncertainty on the cross section is thus calculated as

$$\delta\sigma_{tot}(E) = \sigma_{tot}(E) \left(\frac{\delta N_{Interacting}}{N_{Interacting}} + \frac{\delta N_{Incident}}{N_{Incident}} \right) \quad (4.8)$$

where:

$$\delta N_{Incident} = \sqrt{N_{Incident}} \quad (4.9)$$

$$\delta N_{Interacting} = \sqrt{N_{Interacting} \left(1 - \frac{N_{Interacting}}{N_{Incident}}\right)}. \quad (4.10)$$

4.2.4 Procedure testing with truth quantities

The π^- -Ar and K^+ -Ar total hadronic cross section implemented in Geant4 can be used as a tool to validate the measurement methodology. We describe here a closure test done on Monte Carlo to prove that the methodology of slicing the TPC retrieves the underlying cross section distribution implemented in Geant4 within the statistical error.

For pions in the considered energy range, **the Geant4 inelastic model adopted to is “BertiniCascade”, while the elastic model “hElasticLHEP”**. For kaons, the Geant4 inelastic model adopted to is “BertiniCascade”, while the elastic model “hElasticLHEP”.

For the validation test, we fire about 390000 pions and 140000 kaons inside the LArIAT TPC active volume using the DDMC (see sec 6.1.2). We apply the thin-sliced method on using true quantities to calculate the hadron kinetic energy at each slab in order to decouple reconstruction effects to eventual issues with the methodology. For each slab of 4.7 mm length on the path of the hadron, we integrate the true energy deposition as given by the Geant4 transportation model. Then, we recursively subtracted it from the hadron kinetic energy at the TPC front face to evaluate the kinetic energy at each slab until the true interaction point is reached. Doing so, we obtain the true interacting and incident distributions for the considered hadron and we obtain the true MC cross section as a function of the hadron true kinetic energy.

Figure 4.2.4 shows the total hadronic cross section for argon implemented in Geant4 10.01.p3 (solid lines) overlaid with the true MC cross section as obtained with the sliced TPC method (markers) for pions on the left and kaons on the right; the total cross section is shown in green, the elastic cross section in blue and the inelastic cross section in red. The nice agreement with the Geant4 distribution and the cross section obtained with the sliced TPC method gives us confidence in the validity of the methodology.

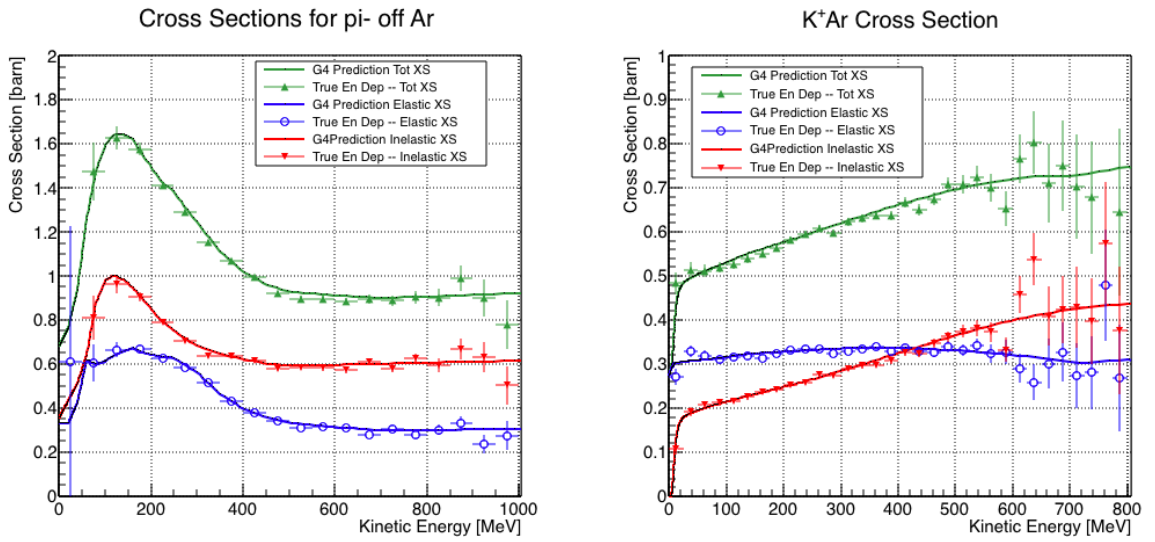


Figure 4.1: Hadronic cross sections for π^- -Ar (left) and K^+ -Ar (right) implemented in Geant4 10.01.p3 (solid lines) overlaid the true MC cross section as obtained with the sliced TPC method (markers). The total cross section is shown in green, the elastic cross section in blue and the inelastic cross section in red.

Chapter 5

Data Collection

Your first chapter is probably an introduction. But who knows.

Chapter 6

LArIAT Monte Carlo

6.1 Beamline

6.1.1 G4Beamline

6.1.2 Data Driven MC

6.2 TPC MC

Chapter 7

Energy Calibration

Your first chapter is probably an introduction. But who knows.

Chapter 8

Tracking Optimization

Understanding how kaons and pions are tracked inside the TPC and optimizing the reconstruction algorithms to maximize the correct identification of the interaction point is a fundamental step of the analysis.

8.1 MC sample and WC2TPC match

The optimization is performed on a MC sample of 191000 kaons and 359000 pions produced with the DDMC technique. DDMC particles are shot from the WC4 location into the TPC following the beam profile. We mimic the matching between the WC and the TPC track on Monte Carlo by constructing a fake WC track using truth information at wire chamber four. We then apply the same WC to TPC matching algorithm as in data.

Plots I want in this section:

1. WC2TPC MC DeltaX, DeltaY and α
2. Delta L, reco - true
3. Delta L, reco - true Elastic, Delta L, reco - true Inelastic, other

4. Length Quality cut
5. Efficiency as a function of true KE and Angle

8.2 Wire chamber-to-TPC match

8.2.1 Wire chamber-to-TPC match: importance and definition

something something about why this match is important

In data, we attempt to uniquely match one WC-Track to one and only one reconstructed TPC track. This match is done by using in the X and Y coordinate of the extrapolated WC-Track to the upstream most point of the reconstructed TPC Track and by using the angle between the incoming track angle and the reconstructed TPC. We define ΔX as the difference between the x position of the most upstream point of the TPC track and the x position of the WC track as projected to the TPC front face. ΔY is defined analogously. We define ΔR as $\Delta R = \sqrt{\Delta X^2 + \Delta Y^2}$. The angle between the incident WC Track and the TPC track in the plane that contains them defines α .

We define a match between WC-track and TPC reconstructed track if $\Delta R < r_T$, $\alpha < \alpha_T$ and the Z position of the first reconstructed point of the TPC track is within 2 cm from the TPC front face. The determination of the best r_T and α_T is the scope of the following section.

In MC, we mimic the matching between the WC and the TPC track on Monte Carlo by constructing a fake WC track using truth information at wire chamber four. We then apply the same WC to TPC matching algorithm as in data.

8.2.2 Matching optimization

Scope of this optimization study is assessing the goodness of the wire chamber-to-TPC match on Monte Carlo and porting the optimized selection cuts to data. A word of caution is necessary here. With this study, we want to minimize pathologies associated with the presence of the primary kaon itself, like the incorrect association between the beamline kaon its decay products inside the TPC. Assessing the contamination from pile-up¹, albeit related, is beyond the scope of this study.

In MC, we are able to define a correct WC2TPC match using the Geant4 truth information. We are thus able to count how many times the WC tracks is associated with the wrong TPC reconstructed track.

We define a correct match if the all following conditions are met:

- the length of the true primary Geant4 track in the TPC is greater than 2 cm,
- the length of the reconstructed track length is greater than 2 cm,
- the Z position of the first reconstructed point is within 2 cm from the TPC front face
- the distance between the reconstructed track and the true entering point is the minimum compared with all the other reconstructed tracks.

In order to count the wrong matches, we consider all the reconstructed tracks whose Z position of the first reconstructed point lies within 2 cm from the TPC front face. Events with true length in TPC < 2 cm are included. Since kaons are shot 100 cm upstream from the TPC front face, the following two scenarios are possible from a truth standpoint:

[*Ta*] the primary kaon decays or interact strongly before getting to the TPC,

1. We remind the reader that the DDMC is a single particle Monte Carlo, where the beam pile up is not simulated.

[Tb] the primary kaon enters the TPC.

Once we choose the selection cuts to determine a reconstructed wire chamber-to-TPC match r_T and α_T , the following four scenarios are possible :

- 1) no reconstructed tracks are matched
- 2) the correct track and one (or more) wrong tracks are matched
- 3) only the correct track is matched
- 4) one (or more) wrong track is matched.

If we keep only events with one and only one match, we discard cases 1) and 2) from the cross section measurement. For each set of r_T and α_T selection value, we define purity and efficiency of the selection as follows:

$$\text{Efficiency} = \frac{\text{Number of events correctly matched}}{\text{Number of events with primary in TPC}} \quad (8.1)$$

$$\text{Purity} = \frac{\text{Number of events correctly matched}}{\text{Total number of matched events}}. \quad (8.2)$$

Figure 8.1 shows the efficiency (left) and purity (right) for wire chamber-to-TPC match as a function of the radius, r_T , and angle, α_T , selection value. It is apparent how both efficiency and purity are fairly flat as a function of the radius selection value at a given angle. This is not surprising, given the fact that the wrong matches can occur in a single particle gun MC only for mis-tracking of the primary or for association with decay products, which are generally different in angle, but might be more similar in x and y projection. The radius cut would play a key role in removing pile up events.

For LArIAT cross section measurements, we generally prefer purity over efficiency, since a sample of particle of a pure species will lead to a better measurement. In the

case of kaons however, efficiency needs not to drop too low, given the smallness of the kaon sample. We choose $(\alpha_T, r_T) = (8 \text{ deg}, 4 \text{ cm})$ and get a MC 85% efficiency and 98% purity.

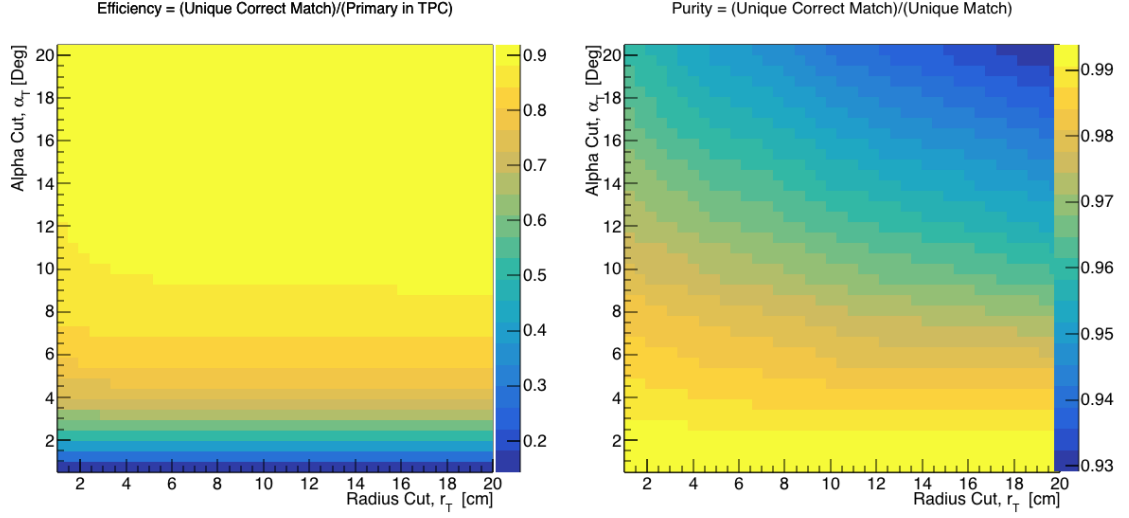


Figure 8.1: Efficiency (left) and purity (right) for wire chamber-to-TPC match as a function of the radius and angle selections.

8.2.3 Porting optimization to data

Chapter 9

Kaon Cross Section Measurement

Your first chapter is probably an introduction. But who knows.

Appendix A

Measurement of LArIAT Electric Field

The electric field of a LArTPC in the drift volume is a fundamental quantity for the proper functionality of this technology, as it affects almost every reconstructed quantity such as the position of hits or their collected charge. Given its importance, we calculate the electric field for LArIAT with a single line diagram from our HV circuit and we cross check the obtained value with a measurement relying only on TPC data.

Before getting into the details of the measurement procedures, it is important to explicit the relationship between some quantities in play. The electric field and the drift velocity (v_{drift}) are related as follows

$$v_{drift} = \mu(E_{field}, T)E_{field}, \tag{A.1}$$

where μ is the electron mobility, which depends on the electric field and on the temperature (T). The empirical formula for this dependency is described in [?] and shown in Figure A.1 for several argon temperatures.

The relationship between the drift time (t_{drift}) and the drift velocity is trivially

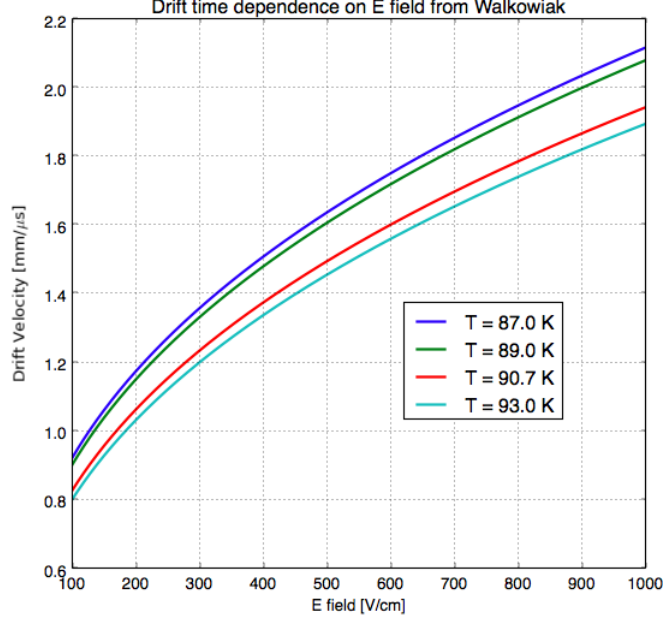


Figure A.1: Drift velocity dependence on electric field for several temperatures. The slope of the line at any one point represents the electron mobility for that given temperature and electric field.

Table A.1: Electric field and drift velocities in LArIAT smaller drift volumes

	Shield-Induction	Induction-Collection
E_{field}	700.625 V/cm	892.5 V/cm
v_{drift}	1.73 mm/ μ s	1.90 mm/ μ s
t_{drift}	2.31 μ s	2.11 μ s

given by

$$t_{drift} = \Delta x / v_{drift}, \quad (\text{A.2})$$

where Δx is the distance between the edges of the drift region. Table A.1 reports the values of the electric field, drift velocity, and drift times for the smaller drift volumes.

With these basic parameters established, we can now move on to calculating the electric field in the main drift region (between the cathode and the shield plane).

Single line diagram method

The electric field strength in the LArIAT main drift volume can be determined knowing the voltage applied to the cathode, the voltage applied at the shield plane, and the distance between them. We assume the distance between the cathode and the shield plane to be 470 mm and any length contraction due to the liquid argon is negligibly small (~ 2 mm).

The voltage applied to the cathode can be calculated using Ohm's law and the single line diagram shown in Figure A.2. A set of two of filter pots for emergency power dissipation are positioned between the Glassman power supply and the cathode, one at each end of the feeder cable, each with an internal resistance of $40\text{ M}\Omega$. The output current of the Glassman power supply is then used to determine the electric field strength. Figure A.3 shows an average current of 0.004172 mA from the Glassman power supply.

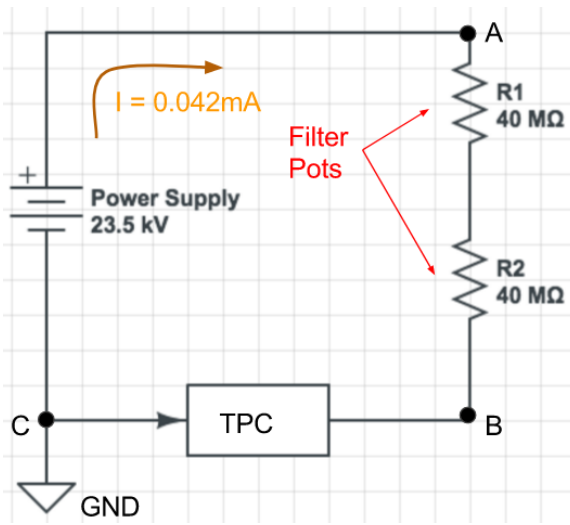


Figure A.2: ~~get rid of current line~~ LAr-IAT HV simple schematics.

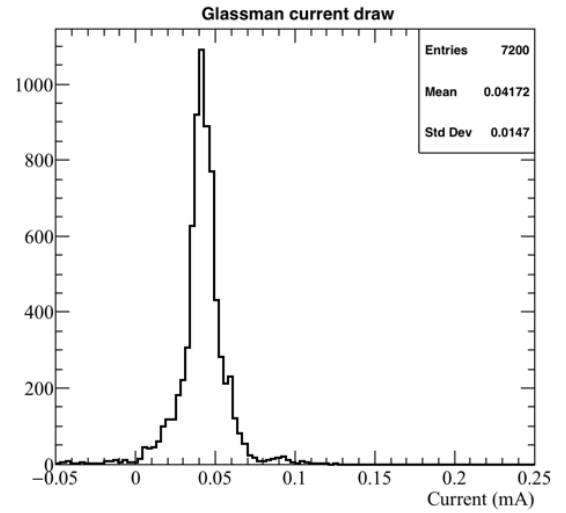


Figure A.3: ~~the axis is wrong!!~~ Current reading from the Glassman between May 25th and May 30th, 2016 (typical Run-II conditions).

Using this current, the voltage at the cathode is calculated as

$$V_{BC} = V_{PS} - (I \times R_{eq}) = -23.5 \text{ kV} + (0.00417 \text{ mA} \times 80 \text{ M}\Omega) = -23.17 \text{ kV}, \quad (\text{A.3})$$

where I is the current and R_{eq} is the equivalent resistor representing the two filter pots. The electric field, drift voltage, and drift time are then calculated to be

$$E_{\text{field}} = \frac{V_{BC} - V_{\text{shield}}}{\Delta x} = 486.54 \text{ V/cm} \quad (\text{A.4})$$

E field using cathode-anode piercing tracks

We devise an independent method to measure the drift time (and consequently drift velocity and electric field) using TPC cathode to anode piercing tracks. We use this method as a cross check to the single line method. The basic idea is simple:

0. Select cosmic ray events with only 1 reconstructed track
1. Reduce the events to the one containing tracks that cross both anode and cathode
2. Identify the first and last hit of the track
3. Measure the time difference between these two hits (Δt).

This method works under the assumptions that the time it takes for a cosmic particle to cross the chamber ($\sim \text{ns}$) is small compared to the charge drift time ($\sim \text{hundreds of } \mu\text{s}$).

We choose cosmic events to allow for a high number of anode to cathode piercing tracks (ACP tracks), rejecting beam events where the particles travel almost perpendicularly to drift direction. We select events with only one reconstructed track to maximize the chance of selecting a single crossing muon (no-michel electron). We utilize ACP tracks because their hits span the full drift length of the TPC, see figure

A.4, allowing us to define where the first and last hit of the tracks are located in space regardless of our assumption of the electric field.

One of the main features of this method is that it doesn't rely on the measurement of the trigger time. Since Δt is the time difference between the first and last hit of a track and we assume the charge started drifting at the same time for both hits, the measurement of the absolute beginning of drift time t_0 is unnecessary. We boost the presence of ACP tracks in the cosmic sample by imposing the following requirements on tracks:

- vertical position (Y) of first and last hits within ± 18 cm from TPC center (avoid Top-Bottom tracks)
- horizontal position (Z) of first and last hits within 2 and 86 cm from TPC front face (avoid through going tracks)
- track length greater than 48 cm (more likely to be crossing)
- angle from the drift direction (phi in figure A.5) smaller than 50 deg (more reliable tracking)
- angle from the beam direction (theta in figure A.5) greater than 50 deg (more reliable tracking)

Tracks passing all these selection requirements are used for the Δt calculation.

For each track passing our selection, we loop through the associated hits in order to retrieve the timing information. The analysis is performed separately on hits on the collection plane and induction plane, but lead to consistent results. As an example of the time difference, figures A.6 and A.7 represent the difference in time between the last and first hit of the selected tracks for Run-II Positive Polarity sample on the collection and induction plane respectively. We fit with a Gaussian to the peak of the Δt distributions to extract the mean drift time and the uncertainty associated with

it. The long tail at low Δt represent contamination of non-ACP tracks in the track selection. We apply the same procedure to Run-I and Run-II, positive and negative polarity alike.

To convert Δt recorded for the hits on the induction plane to the drift time we utilize the formula

$$t_{drift} = \Delta t - t_{S-I} \quad (\text{A.5})$$

where t_{drift} is the time the charge takes to drift in the main volume between the cathode and the shield plane and t_{S-I} is the time it takes for the charge to drift from the shield plane to the induction plane. In Table A.1 we calculated the drift velocity in the S-I region, thus we can calculate t_{S-I} as

$$t_{S-I} = \frac{l_{S-I}}{v_{S-I}} = \frac{4mm}{1.745mm/\mu s} \quad (\text{A.6})$$

where l_{S-I} is the distance between the shield and induction plane and v_{S-I} is the drift velocity in the same region. A completely analogous procedure is followed for the hits on the collection plane, taking into account the time the charge spent in drifting from shield to induction as well as between the induction and collection plane. The value for Δt_{drift} , the calculated drift velocity (v_{drift}), and corresponding drift electric field for the various run periods is given in Table A.2 and are consistent with the electric field value calculated with the single line diagram method.

Delta t_{drift} , drift v and E field with ACP tracks

Data Period	$\Delta t_{Drift} [\mu s]$	Drift velocity $[mm/\mu s]$	E field $[V/cm]$
RunI Positive Polarity Induction	311.1 ± 2.4	1.51 ± 0.01	486.6 ± 21
RunI Positive Polarity Collection	310.9 ± 2.6	1.51 ± 0.01	487.2 ± 21
RunII Positive Polarity Induction	315.7 ± 2.8	1.49 ± 0.01	467.9 ± 21
RunII Positive Polarity Collection	315.7 ± 2.7	1.49 ± 0.01	467.9 ± 21
RunII Negative Polarity Induction	315.9 ± 2.6	1.49 ± 0.01	467.1 ± 21
RunII Negative Polarity Collection	315.1 ± 2.8	1.49 ± 0.01	470.3 ± 21
Average Values	314.1	1.50 ± 0.01	474.3 ± 21

Table A.2: Δt for the different data samples used for the Anode-Cathode Piercing tracks study.

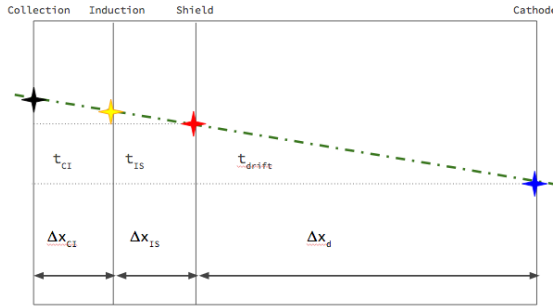


Figure A.4: Pictorial representation of the YX view of the TPC. The distance within the anode planes and between the shield plane and the cathode is purposely out of proportion to illustrate the time difference between hits on collection and induction. A ACP track is shown as an example.

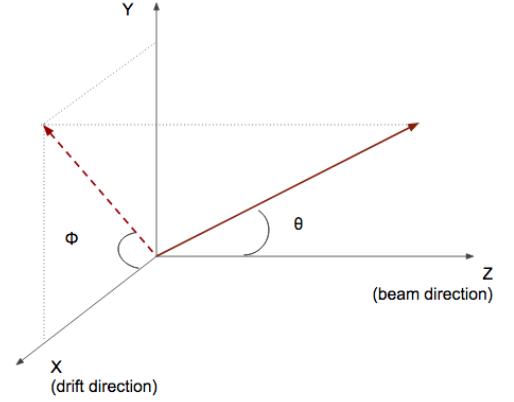


Figure A.5: Angle definition in the context of LArIAT coordinates system.

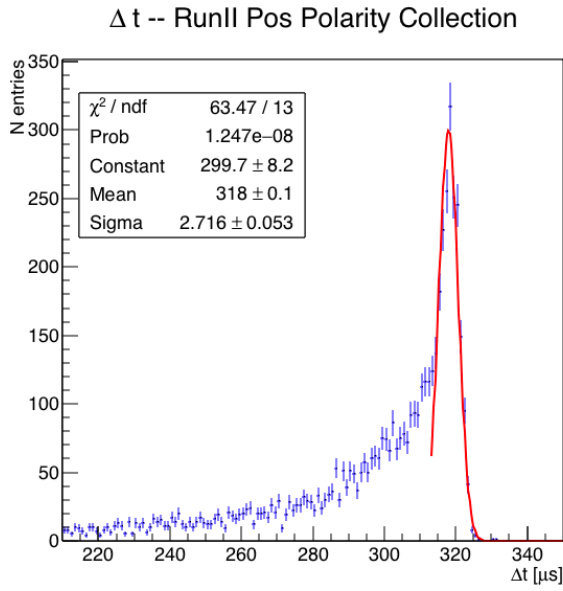


Figure A.6: Collection plane Δt fit for Run II positive polarity ACP data selected tracks.

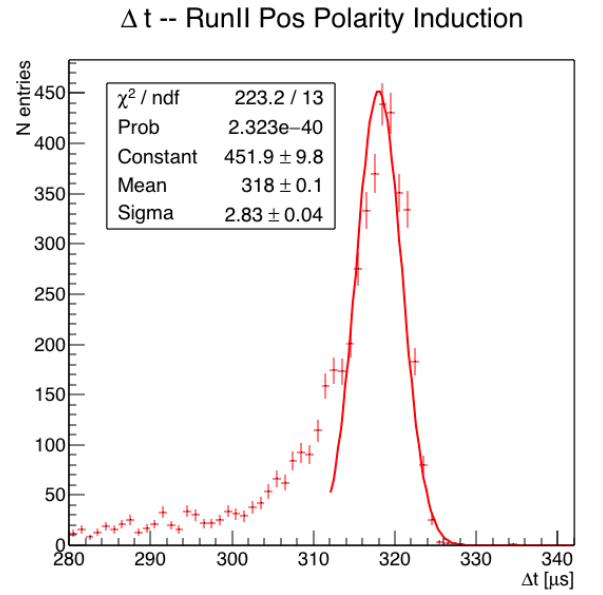


Figure A.7: Induction plane Δt fit for Run II positive polarity ACP data selected tracks.

Appendix B

Construction of A Cosmic Ray

Tagger for MicroBooNE

Appendix C

Pion Analysis

C.0.1 Data Sample

We decided to use only the data from the -60 A, -100 A RunII configurations, because the beam composition for these 2 beamline configurations is available in G4Beamline. Run II data is better than Run I in terms of calorimetry and understanding of the detector.

The used SamWeb definition is PionAna.RunII_60A_100A_lovely1_elenag_00 =
Defined as “defname: Lovely1 and data_tier digits and lariat_mid_f_mc7anb ; 0
and create_date ; '2017-06-02' and run_number != 9276 and run_number != 9277
and run_number != 8836 and run_number != 9083 and run_number != 9122 and
run_number != 8977 and run_number != 8981 and run_number != 8982 and run_number
!= 8983 and run_number != 8984 and run_number != 8985 and run_number != 8991
and run_number != 8994 and run_number != 8996 and run_number <= 8767 and
run_number >= 9635”

C.0.2 Capture and Decay

Our goal is to measure the total hadronic cross section for negative pions in argon. Since pion capture can be classified as an electromagnetic process and pion decay is

Table C.1: My caption

Stage	-100A +64 GeV	-60A +64 GeV	Number of Evt
SamWebDefinition	32.7%	67.3%	3569206
WCQuality	37.8%	63.2%	553486
$P_{WC4} > 420 \text{ MeV/c}$	50.8%	49.2%	423294
TOF Cut	32.7%	67.3%	

a week process, capture and decay represent unwanted interactions in our sample. We present here a study of capture and decay in Monte Carlo and the solution we adopted to mitigate their present in our sample.

For this MC study, we use a sample of 359000 MC pions generated according to the beam profile with the DDMC described in 6.1.2. Unlike decay – which may occur both in flight and at rest – capture occurs predominantly at rest. Thus, we can highly mitigate capture and decay at rest by removing pions whose energy is low enough to stop in the TPC. This translates into a momentum selection, where we keep only events whose WC momentum is above a certain threshold. Figure C.1 shows the true momentum distribution for the primary¹ pions that arrive to the TPC (pink), that capture (green) or decay (blue) inside the TPC, on a linear and log scale vertical axis.

In order to choose the selection value for the wire chamber momentum, it is beneficial to estimate the ratio of events which capture or decay that survive the selection in MC as a function of the momentum threshold, and compare it with the survival ratio for all events. This is done in figure C.2. We define the survival ratio simply as the number of events surviving the true momentum cut divided by the number of events of that given category. The survival ratio calculated separately for the three event categories explained above: total (pink), capture (green) and decay (blue). Selecting pions with momentum greater than 420 MeV/c reduces the capture

1. We use here the Geant4 denomination "primary" to indicate that the pion considered does not undergo interactions modifying its energy before getting to the TPC. In fact, not every pion shot from wire chamber four will arrive to the TPC as primary, some will decay or interact before the TPC, as explained in [reference to WC 2 TPC chapter](#)

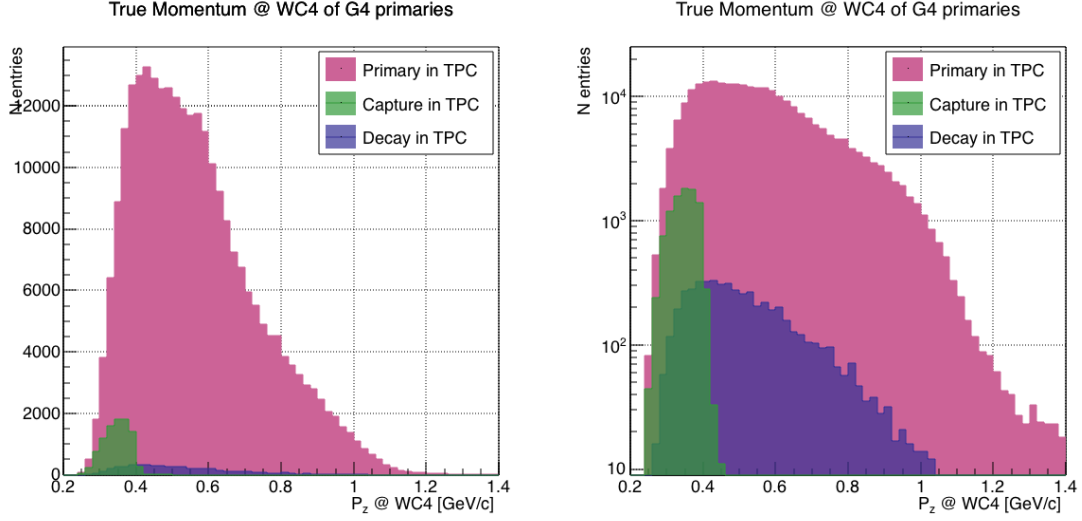


Figure C.1: True momentum distribution at wire chamber 4 for every simulated pion arriving in the TPC (pink), ending its life in capture (green) or in decay (blue) in the TPC, linear vertical axis on the left, logarithmic on the right.

events by 99% while maintaining about 80% of the total data sample. Figure C.3 shows the ratio of events which end their life in capture (green) or decay (blue) over the total number of events as a function of the true momentum at wire chamber four. This ratio is slightly dependent on the inelastic cross section implemented in Geant4, as we are able to register a pion capture (or decay) only if it doesn't interact inelastically in the TPC. For momenta greater than 420 MeV/c, the percentage of capture events drops below 1% and the percentage of decays is never above 2%.

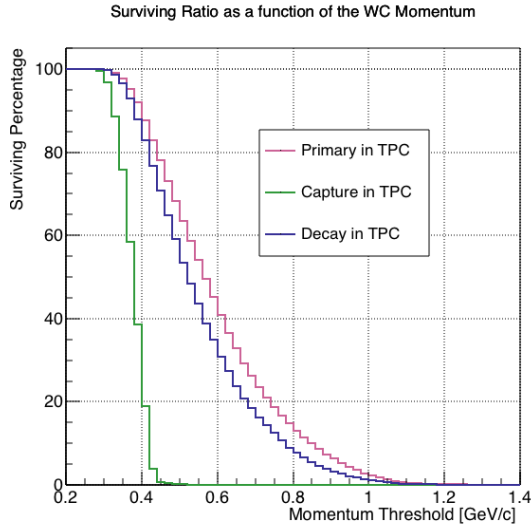


Figure C.2: Survival ratio as a function of selection threshold on true momentum at wire chamber four for every simulated pion arriving in the TPC (pink), capture (green) or in decay (blue).

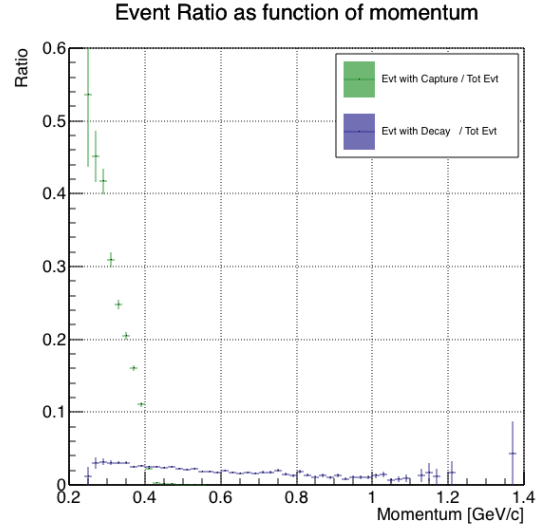


Figure C.3: Ratio between the capture (green) and decay (blue) events over the total number of events as a function of the true momentum at wire chamber four.

Bibliography

- [1] Peter W. Higgs. Broken symmetries and the masses of gauge bosons. *Physical Review Letters*, 13(16):508–509, oct 1964.
- [2] P.W. Higgs. Broken symmetries, massless particles and gauge fields. *Physics Letters*, 12(2):132–133, sep 1964.
- [3] Steve Ritz et al. Building for Discovery: Strategic Plan for U.S. Particle Physics in the Global Context. 2014.